Northumbria Research Link

Northumbria
University
NEWCASTLE

Ever-increasing pseudocapacitance in RGO-MnO-RGO sandwich nanostructure to dominate rate performance for ultrahigh-rate lithium storage

Tianzhi Yuan[1], Yinzhu Jiang[1], Ben Xu[2], Bo Xiang[1], Yong Li[1], Mi Yan[1*]*

[1] *State Key Laboratory of Silicon Materials, Key Laboratory of Advanced Materials and Applications for Batteries of Zhejiang Province, Department of Materials Science and Engineering, Zhejiang University, Hangzhou 310027, China*

[2] *Smart Materials and Surfaces Lab, Faculty of Engineering and Environment, Mechanical Engineering, Northumbria University, Newcastle upon Tyne, NE1 8ST, UK*

[*] Correspondence authors: *yzjiang@zju.edu.cn* (Y. Jiang), *mse_yanmi@126.com* (M. Yan)

The increasing demand in environment-friendly electric vehicles (EVs) and hybrid electric vehicles (HEVs) has driven the development of lithium-ion batteries (LIBs) for stronger power, higher energy and longer lifespan. By now, there still considerable gaps exist on the related power attributes for the current LIBs (mostly graphite anodes based), mainly due to the limited Li-ion diffusion coefficient and potential operational risks at a high charge-discharge rate. To achieve higher performance, significant efforts have been devoted to exploit alternative structural electrode materials in last decade, to reduce Li-ion diffusion length within the solid electrodes, increase electrode/electrolyte contact area and improve interfacial kinetics, where the diffusion of Li-ions in and out of the electrodes are normally considered as kinetically dominated. Pseudocapacitors, an electrical energy store structure with fast Faradic surface redox reactions, could achieve high power density, long lifetime but low energy density. It would be very interesting to develop novel electrode materials to enable fast surface redox reactions and diffusion-controlled Li-ions insertion/extraction in a single electrochemical energy storage device, to achieve battery-like capacity and supercapacitor-like power at the same time.

Transition metal oxides (TMOs, *e.g.*, CoO, NiO, Fe_2O_3, MnO and MoO_3), known as promising anode materials of LIBs, could present unique higher reversible capacities than graphite *via* conversion reactions. Pseudocapacitive-like storage behaviors have been previously observed in TMO-based anodes of LIBs, with presenting surface redox and diffusion controlled energy storage simultaneously. Brezesinski *et al.* prepared iso-oriented α-MoO_3 mesoporous film, which enables Li-ions to be inserted into the van der Waals gaps (intercalation pseudocapacitance) in addition to slow diffusion of Li-ions through the bulk of α-MoO_3. The extra pseudocapacitive reaction offers high power while sustaining energy density of LIBs.

In our previous work, we achieved the similar enhanced capacitive behavior upon cycling hierarchically porous amorphous Fe_2O_3 anode, a large capacity increment was witnessed at a high current density of 1 A g^{-1}. Such surface capacitive storage effect has been very limited exposed since it was normally shadowed and influenced by the structure design and surface chemical evolution of the electrode. It has been limited understood, the traceable hypothesis assume that it was originated from the refinement effect and deep oxidation of TMO-based anodes.

In the current report, we explore a new strategy to achieve ultrahigh rate lithium storage with a nanostructural RGO-MnO-RGO sandwich anode, in which surface redox capacitive contribution and diffusion controlled lithium storage are dynamically balanced through the structural sandwich design and the self-adaption of its microstructure during cycling. The surface RGO layers (top-covered and foundation) create fast pathway for electron transfer and suppress the possible stress localization from lithiation/delithiation; Moreover, a "pocket" constructed by the double RGO layers could favorably trap the refined manganese oxide nanaoparticles and effectively constrain the aggregation of active materials, leading to the self-adaption in microstructure and thus forming RGO-wrapped hierarchical manganese oxide nanoclusters. We successfully validate ever-increasing surface capacitive storage in MnO-based anodes of LIBs, with rate capability (331.9 mAh g^{-1} at 40 A g^{-1}, 391 mAh g^{-1} after 4000 cycles at 15 A g^{-1}) and outstanding cycle stability.

Results

The electrodepositing fabricated RGO-MnO-RGO sandwich nanostructures are illustrated in Figure S1, the morphology of each layer was recorded for multi-layered sandwich nanostructures with field-emission scanning electron microscopy (FESEM).

Figure 3a-c show typical FESEM images of foundational RGO film deposited on stainless steel plate. After carrying out electrodeposition in combination with reduction by using hydrazine, steel plate is uniformly covered by the RGO film with the visible characteristic of semi-transparence and textures. The elemental purity and chemical homogeneity of GO/RGO layer were verified with Raman spectrum (G band ~1593.8 cm^{-1}, D band ~1345.9 cm^{-1}, Figure 2a) and high-resolution C1s XPS spectrum (284.6 eV for C-C, 286.2 eV for C−O and 289.0 eV for O-C=O, Figure 2b). The RGO layer will not only enhance the electron transfer of electrode, but also act as a flexible substrate to release the internal stress and inhibit the aggregation of magnaneous oxide grains during cycling.

After electrodepositing MnO, interconnected MnO nanorods (diameter in the range of 15-30 nm) with random orientation are attached on the surface of the bottom RGO layer (Figure 3d-f)). The X-ray diffraction (XRD) patterns of the pure Mn_xO_y film (Figure 2d) present a clean scan except for the background diffraction peaks from stainless steel substrate. After annealed at 600 °C for 6 h in H_2/Ar atmosphere, the XRD patterns can be readily indexed to a pure phase of cubic MnO (JCPDS No: 07–0230). The formation of MnO phase can be identified from Mn 2p XPS spectrum in Figure 2e, with two typical signals at 641.2 eV for Mn $2p_{3/2}$ and 652.9 eV for Mn $2p_{1/2}$. The corresponding energy-dispersive X-ray spectroscopy (EDS) elemental mappings of the layered RGO-MnO nanostructure (Figure S2) suggest uniform distribution for both RGO sheets and MnO nanorods.

Once covering with the top RGO layer, we observe a porous MnO layer (about 400 nm in thickness, Figure S3) packed by rod-like nanoparticles. The high porosity between the interconnected MnO nanoparticles could expand the contact area of electrolyte, preserves voids for Li-ion induced expansion and buffers the strain from

the volume change during cycling. The observations in Figure 3g-i indicate that most area of the MnO layer has been covered by the top RGO film, only leave a small fraction of MnO nanoparticles to be exposed. The top-covered RGO layer can be easily distinguished from its characteristic textures; meanwhile, we can also observe the undercover MnO layer through the semitransparent region of the RGO layer. The distribution of carbon aligns with the outline of the top RGO layer (Figure S4,). The elemental mapping images of Mn and O further demonstrates that MnO nanoparticles are homogeneously grown onto the foundation RGO layer.

This multi-layered sandwich nanostructure offers high mechanical stability as the young's module of GO is much higher than that of MnO (E_{GO} ~ XXX, E_{MnO} ~ XXX), also this structure prevents MnO from disintegration and detaching from RGO film during charge/discharge processes. Without sandwich structure, the electrodeposited bare Mn_xO_y film on the stainless steel substrate shows a porous state with interconnected nanoflakes with ~ 20 nm in thickness (Figure S5a-c). After thermal annealing at XXX ºC, the MnO nanoflakes turned into rod nanoparticles with a dramaticalu reduction in porosity and structure stability (Figure S5d-f).

We further observe RGO-MnO-RGO materials under transmission electron microscopy (TEM). As shown in Figure 4a-c, RGO sheets are intensively decorated with MnO nanoparticles, with an average distribution size of MnO less than 20 nm, which is much smaller than that of bare MnO (Figure S6). The smaller nanoparticle size could dramatically reduce Li-ion transport paths. It should be noted that the measured lattice spacings of 0.255 and 0.221 nm as shown in Figure 4d are in good agreement with the (111) and (200) interplanar distances of MnO phase. The corresponding selected-area electron diffraction (SAED) pattern also reveals the polycrystalline nature of the obtained MnO nanoparticles.

To evaluate the electrochemical lithium-storage properties of RGO-MnO-RGO electrodes, we use cyclic voltammetry (CV) to scan for the initial four cycles (Figure 5a) and compare with bare MnO and RGO-MnO electrodes. An irreversible reduction peak at around 0.72 V appears in the first catholic sweep, corresponding to the irreversible reduction of electrolyte and the formation of a solid electrolyte interphase (SEI) layer. The sharp cathodic peak close to 0.1 V could refer to the complete reduction of Mn^{2+} to Mn^{0}, which shifts significantly to 0.25 V in the second cycle. It's worth noting that this reduction peak further shifts to higher voltage in the following cycles, along with the increase of peak intensity, this could be caused by the improved reaction kinetics resulting from the microstructure transformation. The oxidation peak centered at 1.26 V refer to the reversible oxidation of Mn^{0} to Mn^{2+}. Interestingly, there is an oxidation peak at 2.1 V, which becomes stronger along with cycling, indicating that MnO in RGO-MnO-RGO electrode have been probably oxidized to a higher oxidation state. The deep oxidization of MnO is normally considered as one of the sources to increase capacity. Whereas, the Mn^{2+} ions in bare MnO electrode can not be oxidized to a higher oxidation state anymore, as shown in Figure 4 (b).

We next compare the cycling performances of electrochemical cells with bare MnO, RGO-MnO and RGO-MnO-RGO anode at various current densities (*e.g.*, 0.5 A g^{-1} and 1 A g^{-1}). As it can be seen from Figure 4c, the initial reversible capacity of the RGO-MnO-RGO electrode is 742.3 mAh g^{-1} at 0.5 A g^{-1}. After 200 cycles, a reversible capacity reaches 1172.4 mAh g^{-1}, which is more than three folds of the theoretical capacity of graphite (~372 mAh g^{-1}). It is also much higher than the referenced capacities of MnO (~756 mAh g^{-1}) and graphene (~744 mAh g^{-1}) [].At 1 A g^{-1}, the first discharge and charge capacity of RGO-MnO-RGO nanocomposite are

1038.7 and 657.9 mAh g^{-1}, acquiring an initial Coulombic efficiency of 63.3%. The initial irreversible capacity loss mainly due to the formation of SEI layer, and the reaction of remaining oxygen-containing functional groups on RGO with Li-ions. At the 50th cycle, the discharge capacity of RGO-MnO-RGO, RGO-MnO, and bare MnO is 931.9 mAh g^{-1} (125.5% retention of the initial discharge capacity), 646.9 mAh g^{-1} (123.3% retention of the initial discharge capacity), and 617.0 mAh g^{-1} (106.2% retention of the initial discharge capacity), respectively. The ascending trend of capacity boosts in RGO-MnO-RGO and RGO-MnO are much vigorous than that of bare MnO, which should be related to the incorporation of RGO. Hierarchical incorporating RGO layers could mechanically buffer MnO's expansion during lithiation, prevent the MnO NPs detaching from the electrode and thus stabilize the multilayered structure, as well as fulfill high electrical conductivity for the electrode, ensure full accessibility for lithium insertion and extraction.

In Figure 4d, the corresponding discharge-charge voltage profiles of RGO-MnO-RGO electrode indicate that, during the initial discharge process at 1 A g^{-1}, a long voltage plateau at about 0.1 V can be observed for the reduction of Mn^{2+} to Mn^{0}, whereas for the first charge process, the observed slope between 1.0 and 1.5 V is associated with the reversible oxidation of Mn^{0} to Mn^{2+}. Starting from the second cycle, the discharge plateau has shifted to about 0.45 V, which agrees well with the CV results. It is worth noting that a slope of 1.5−2.2 V in the charge process appears gradually, which might be originated from the further oxidation of Mn^{2+} to a higher oxidation state. The XRD pattern for RGO-MnO-RGO electrode after 50 cycles reveals the formation of Mn_3O_4 (Figure S8). With more cycling, the slope becomes more gently reminding that more capacity to accommodate the extra electrochemical oxidation. After 200 cycles, a large reversible capacity of 1115.7 mAh g^{-1} is obtained.

We assessed the durability for the electrode made by different materials, by using FESEM to observe the tested samples (the fully charged at 3.0 V, following 1 A g^{-1} for 50 cycles). Severe agglomeration of nanoparticles are found for bare MnO, along with the mechanical failure as large cracks appeared on the electrode film (Figure S9a-b), which could lead to electrical disconnection and capacity decay. For RGO-MnO electrode, some micro-cracks are also noted, but overall MnO is well attached to the foundation RGO layer and sustain stable porous structure in nanometer scale (Figure S9c-d). We also found that the upper part of MnO layer with no coverage of RGO sheets aggregated into large spherical particles, this could result in the loss of active materials by volume shrink. For the RGO-MnO-RGO electrode with RGO layers protected (Figure S9e), a hierarchical framework can be identified, which prevent MnO against disintegration and detaching from the electrode, maintaining excellent cycling performance in LIB applications. The MnO without sandwich structure degrades into two kinds of different morphology after 50 cycles (Figure S9 (e), the magnified SEM images are shown in Figure S10).

The evolution of morphology and structure for RGO-MnO-RGO electrode is a key to influence the electrochemical properties. After 50 cycles at discharge state under 15 A g^{-1}, the overall morphology is well maintained, with slightly agglomeration of large nanocrystals (Figure S16). When discharging for 500 times, fine manganese nanoparticles (less than 5 nm) are homogeneously dispersed on the RGO matrix, while the MnO domains are absent (Figure S17). With further 500 cycles at discharge state, most of the active materials transform to be amorphous (Figure S18). Correspondingly, after 50 complete cycles, large MnO nanoparticles are embedded in the RGO matrix with few Mn_3O_4 domains formed at their boundaries (Figure S19). Keeping charge for 500 cycles, we find that lots of Mn_3O_4 nanoparticles appeared

(less than 5 nm) (Figure S20). This is the first direct observation of the transformation of MnO to Mn_3O_4 during the charge process in MnO-based electrodes. We also find that large MnO particles broken and turn into smaller grains after 500 more cycles (Figure S21), which partially mitigate the volume change, reduce the Li-ions transport path and contribute more surface area for capacitive storage.

A key advantage in this context is the superior cycling performance of the RGO-MnO-RGO electrode, even at higher current densities (first cycled five times at a current density of 0.2 A g^{-1} and then cycled up to 500 times at 2 A g^{-1} or 5 A g^{-1}). This can be traced in Figure 4e as the discharge capacity reaches 1269.2 mAh g^{-1} after 500 cycles at 2 A g^{-1}. Even at a current density of 5 A g^{-1}, RGO-MnO-RGO nanostructure delivers a reversible capacity of 964.7 mAh g^{-1} after 500 discharge/charge cycles, where the reversible capacity constantly drops to 347.5 mAh g^{-1} for bare MnO electrode. From the corresponding discharge and charge curves at 5 A g^{-1} (Figure S11), RGO-MnO-RGO and RGO-MnO electrodes both show a gradually increased slope of 1.5-2.2 V in the charge process, leading to the increase of capacity, which we cant find similar trace for bare MnO electrode. We also notice the shift of the main reduction peak forbare MnO from ~0.59 V at the 15^{th} cycle to 0.37 V in 30^{th} cycle (inset of Figure S11), indicating the aggravated polarization of electrochemical reaction during cycling. There is no peak shift seen in *dQ/dV* curves for RGO-MnO-RGO and RGO-MnO electrodes. This means that, with structurally binding RGO layers, the integrity of the multilayer electrodes have been effectively preserved. The structural enhanced electrochemical behavior could also be traced from EIS spectra of the electrodes (Figure S12), where RGO-MnO-RGO electrode exhibits a much lower resistance than RGO-MnO and bare MnO, as a benefit from the enhanced electronic conductivity from RGO. Enhancement of the reaction kinetics is

beneficial for Mn^{2+} ions in RGO-MnO-RGO electrode to be oxidized to a higher oxidation state, leading to fast redox surface reactions and higher reversible capacity. With the sandwich structure, the morphology of the electrodes are well preserved with no crack observed even after 100 cycles at 5 A g^{-1} (Figure S13).

We further investigate the long-term capacity stability at high current density, RGO-MnO-RGO electrode was tested at 15 A g^{-1} for 4000 cycles. The capacity remains at 391 mAh g^{-1}, indicating only 0.003% capacity loss per cycle (Figure 4f). The rate capability test of RGO-MnO-RGO electrode show a results of up to 40 A g^{-1} (Figure 5a), the discharge and charge process finished in about 28 seconds, comparable to the discharge/charge time scale in supercapacitors, with a favorable capacity of 331.9 mAh g^{-1} at a current density of 40 A g^{-1}. While the capacity of bare MnO decreased at each current density higher than 2 A g^{-1} and is only 137.5 mA g^{-1} at 15 A g^{-1}. A reversible capacity of 1151.4 mAh g^{-1} was achieved after 9 cycles when the current density returned to 0.5 A g^{-1}, representing a good cycling stability for RGO-MnO-RGO electrode. Overall, this is an excellent rate performance for MnO-based anode materials.

From the discharge–charge profiles for RGO-MnO-RGO (Figure 5b) and bare MnO (Figure 5c) electrodes, and average discharge and charge potentials of the electrodes in Figure 5d, we found that the polarization of RGO-MnO-RGO electrode at high current densities increases much less than bare MnO, indicating an enhanced reaction kinetics caused by the three-dimensional RGO conductive network. Figure 5e shows the calculated Ragone plots of RGO-MnO-RGO and bare MnO electrode. The energy density of RGO-MnO-RGO electrode is 418.1 Wh kg^{-1} where the power density is 510.6 W kg^{-1}. Even the power density is as high as 15932.6 W kg^{-1}, the energy density can unprecedentedly maintain 123.9 Wh kg^{-1}. For comparison, the

power density of bare MnO decreased to 44.6 Wh kg^{-1} at a power density of 4221.7 W kg^{-1}. Comparing with other anode materials on the basis of half-cell test, the RGO-MnO-RGO electrode presents much higher power and energy densities for high performance LIB devices.

4. Discussion

The 'capacitive' charge storage mechanism dominates the superior electrochemical performance of the RGO-MnO-RGO electrode, as it can be visibly identified from the discharge-charge voltage profiles (Figure S14a-b) for the initial five cycles at 0.2 A g^{-1}. With the current density increased to 15 A g^{-1}, the plateaus still exist for next 200 cycles. After 1000 cycles, the charge/discharge curves are nearly inclined in shape with good symmetry, exhibiting a typical characteristic of supercapacitor. Starting from the 50^{th} cycle, the Z'–Z″ curves at low frequencies become increasingly steeper (Figure S15), representing that the capacitive-like behavior are strengthened. Meanwhile, the radius of the semicircle becomes smaller at high frequencies as a result of the charge transfer resistance, means the enhancement of the electron/ion transport on the electrode/electrolyte interface.

It is important to verify where the ever-increasing pseudocapacitance originates. The XPS results indicates that, after 50 cycles at charge state, from the surface (0 s etched) of RGO-MnO-RGO electrode to the interior (70 s etched), there is a typical Mn $2p_{3/2}$ peak fixed at 641.4 eV (Figure S22a) for MnO. The Mn $2p_{3/2}$ peak centered at 641.6 eV without etching and then gradually shifted to 641.3 eV along with the continuously etching (Figure S22b). The difference in binding energy between the surface and the interior of the sample illustrates that manganese oxide on the surface is in the form of Mn_3O_4. In the CV curves of RGO-MnO-RGO electrode, the cathodic peak corresponding to the Mn^{2+} to Mn^0 shifted to near 0 V because of polarization

(Figure S23a). Upon increasing cycle number (at 15 A g^{-1}), the intensity of the peaks related to the conversion reaction of MnO to Mn gradually decreases. Notably, there appears a new pair of peaks corresponding to the redox reactions between MnO and Mn_3O_4 with gradually strengthened intensity. Therefore, the superior long-term cyclability should be the result of the dynamic equilibrium of the dying conversion reaction and the growing redox reaction.

There is a power law relationship between current (i) and the scan rate (v), $i = av^b$, when electrode materials were tested at various sweep for voltammetric response. When b =0.5, the peak current exhibits a linear relationship with the square root of the sacn rate ($v^{1/2}$), which is considered as a typical diffusion-controlled lithium storage process. When b =1, the peak current is proportional to the scan rate, revealing a surface-controlled charge storage behavior. The voltammetric behavior (from 20 to 150 mV s^{-1}, Figure S23b) of RGO-MnO-RGO after 1000 cycles is used to analyze the charge storage mechanism. The relationships between i and $v^{1/2}$ for peak 1 (conversion reaction of MnO to Mn) are linear (Figure S23c), reflecting a typical diffusion-controlled battery behavior. The b value for the currents of peak 2 and 2′ is ca. 1 (Figure S23d), explicitly suggesting that the kinetics of the redox reactions between MnO and Mn_3O_4 are surface controlled. We also tested the cycled RGO-MnO-RGO electrode in aqueous electrolyte to check the capacitance. Compared to the negligibly small capacitance (19.7 F g^{-1} at 10 mV s^{-1}) of standard pristine electrode (Figure S24a), the capacitance of RGO-MnO-RGO electrode reach up to 282 F g^{-1} (at a scan rate of 10 mV s^{-1}, Figure S24b-c) after 500 cycles (at 5 A g^{-1}). Together with the results of spectrum measurements, it is confirmed that the pseudocapacitance originates primary from the growing redox reactions between MnO and Mn_3O_4.

The surface-controlled capacitive behavior in TMO-based anode materials could be strongly dependent on the electrode structure design and evolution. The FESEM observation indicate that, after 50 cycles at 15 A g^{-1}, the sandwich nanostructure was preserved with a slight agglomeration of manganese oxide (Figure S25a-c). Similar to the sample cycled at 5 A g^{-1} for 100 times, the surface of the top RGO layer are densely decorated by manganese oxide nanoparticles, avoiding the detachment of active materials. The RGO-MnO-RGO sandwich structure converted into RGO-wrapped nanoclusters completely after 500 discharge/charge cycles (Figure S25d-f), the middle hierarchical nanoclusters composing of small manganese oxide nanoparticles are attached tightly to RGO sheets. This will increase the proportion of the total active materials on the surface of RGO sheets, thus leading to a larger specific surface area and facilitating charge transfer. When the morphology and structure of RGO-MnO-RGO electrode further evolves, more pristine MnO will be oxidized to fine Mn_3O_4 nanoparticles, resulting in the increase of pseudocapacitance.

The self–adaption process of RGO-MnO-RGO electrode at large current densities is illustrated in Figure 6. At a high current density of 15 A g^{-1}, “electrochemical sintering” leads to the aggregation and detaching of MnO nanoparticles from the current collector in the first few hundred cycles. For bare MnO electrode, such aggregation results in the loss of active materials and capacity decay (Figure 5a). However, the RGO layers in RGO-MnO-RGO electrode could effectively trap the detached manganese oxide due to its better electrical conductivity and residual oxygen-containing functional groups. Furthermore, along with continuous cycling, sandwich nanostructure could completely convert to RGO-wrapped manganese oxide hierarchical nanoclusters by the self-adaption of RGO-MnO-RGO electrode (Figure 5b). With increased specific surface area created by the self-adaption, closer

connection with RGO matrix and smaller size of manganese oxide grains, electronic/ionic conductivity of the electrode could be achieved. A number of MnO could be oxidized reversibly to Mn_3O_4 via a fast surface-controlled redox reaction, leading to ever-increased pseudocapacitive contribution and excellent rate capability.

By designing the materials and nanostructure, we can bridge the gap between LIBs and supercapacitors by using Li-ion hybrid capacitors, the dynamic equilibrium of the surface redox reaction (*e.g.,* nonFaradic reversible ion adsorption and fast Faradic surface redox reactions) and the diffusion-controlled conversion reaction (e.g., Li-ions insertion/extraction) in RGO-MnO-RGO electrode surprisingly achieves the goal of high power (Figure 5b) and energy densities (Figure 5c) synchronously (Figure 5d).

High storage capacity, good cycling stability, and superior rate capability were obtained for RGO-MnO-RGO electrode. First, the porosity between the interconnected MnO nanoparicles contributes positively to Li-ion diffusion, and provides more void space to prevent the volume expansion/contraction upon cycling. Second, highly flexible and stable RGO framework acts as a buffer matrix that restrains the aggregation of MnO effectively, improving the mechanical reinforcement of the overall electrode. Third, the outmost RGO layer can prevent MnO detached from bottom RGO layer during discharge/charge processes, maintaining the integrity and stability of the overall electrode and improves its cyclability. Finally, three-dimensional RGO network offers a conductive enhancement for ionic and electronic transport. With all these advantages, as the main source of specific capacity, diffusion-controlled conversion reaction is facilitated at relative low current density ($< 5Ag^{-1}$). At higher current density ($\geq 5Ag^{-1}$), through the self-adaption of RGO-MnO-RGO electrode, the ever-increasing pseudocapacitive charge storage of manganese oxide can be fully used, which contribute to the much improved rate

capability.

In summary, the RGO-MnO-RGO sandwich nanostructures were fabricated by layer-by-layer electrodepositon, the RGO layers enables protection of the active MnO layer against the aggregation and volume changes, as well as increases the ionic/electrical conductivity for the electrode. Benefit from the designed sandwich structure, pseudocapacitance effect was generated by the surface redox reactions, yield excellent cycling performance (1115.7 mAh g^{-1} over 200 cycles at 0.5 A g^{-1}, 946.7 mAh g^{-1} over 500 cycles at 5 A g^{-1}) and superior rate capability (331.9 mAh g^{-1} at 40 A g^{-1}, 391 mAh g^{-1} after 4000 cycles at 15 A g^{-1}) when the proposed materials was used as anode material for lithium storage. The unique design of the RGO-MnO-RGO electrode embedded with proposed ever-increased pseudocapacitance effect could store/deliver high energy at ultra-high rates with excellent stability, might open the window for next generation anode materials for high energy/power-density applications.

Methods

Material Preparation

The GO was prepared from natural graphite powder by a modified Hummer's method. The foundation GO layer grown on stainless steel plate (2×2 cm^2) by electrodepositing for 45s. Afterward, the GO film was placed in a petri dish filled with hydrazine monohydrate (2 mL) at 50 ºC for 12 h to form a RGO film. Then, Mn_xO_y layer was deposited onto the RGO-coated stainless steel plate. The anodic electrodeposition was conducted in an aqueous solution (100 mL) containing manganese acetate (0.1 M) and sodium sulfate (0.1 M) at 1.0 V for 600 s at 40 ºC. Bare Mn_xO_y film was deposited directly on stainless steel plate under the same conditions. The top cover layer of GO was coated on the fabricated RGO-Mn_xO_y layered structure using the above process to achieve foundation GO layer. The only different parameter is the mass of GO in the suspension was increased to 15 mg to obtain a uniform GO film. The as-prepared RGO-Mn_xO_y-GO film was then annealed in a tube furnace at 600 ºC for 6 h in H_2 (5%)/Ar (5 ºC min^{-1}) to achieve the RGO-MnO-RGO product.

Chemical structure and morphology characterization

The crystal structures of electrode materials were characterized by X-ray diffraction (XRD) on a Rigaku D/Max-2550pc diffractometer equipped with Cu K_α radiation (λ = 1.5406 Å), with a scan range of 20-80º. The Raman spectrum was recorded on a Renishaw inVia Raman Microscope (532 nm). X-ray photoelectron spectroscopy (XPS) measurements were conducted on an ESCALAB 250 X-ray photoelectron spectrometer, using excitation energy of 1486.6 eV (Al Ka). The structure and morphology of the samples were analyzed by field-emission scanning electron microscopy (FESEM, Hitachi S-4800) and transmission electron microscopy (TEM,

FEI Tecnai G^2F20 microscope). The selected area electron diffraction (SAED) patterns were measured using a FEI Tecnai G^2F20 microscope. The accelerating voltage was set to 200 kV.

Electrochemical characterization

The electrochemical behavior was assessed in CR2025 coin-type cells, using the as-prepared films on stainless steel plates (1×1 cm^2) as the working electrode and lithium foil as the counter and reference electrode, respectively. Celgard 2300 microporous polypropylene was used as the separator. The electrolyte was 1 M $LiPF_6$ solution in a 50:50 v/v mixture of ethylene carbonate (EC) and diethyl carbonate (DEC). Cell assemble was carried out in an Argon filled glove box, where both oxygen concentration and moisture level were maintained less than 1 ppm. The cells were galvanostatically charged and discharged on a Neware BTS-5V10mA battery cycler at 0.005-3 V (vs. Li/Li^+). Cyclic voltammetry (CV) tests in non-aqueous electrolyte were conducted on a CHI660C electrochemistry workstation between 0.005 and 3.0 V (vs. Li/Li^+) at various scan rates. For the CV tests in aqueous electrolyte, three-electrode configuration was applied. The working electrodes (1×1 cm^2) were the pristine or cycled RGO-MnO-RGO electrodes in LIBs. Platinum plate was **used** as the counter electrode and saturated calomel electrode (SCE) as the reference electrode. The applied potential window was ranged from 0 V to 0.8 V in a 1 M Na_2SO_4 electrolyte. In the electrochemical impedance spectroscopy (EIS) measurements, the applied excitation voltage was 5 mV and the frequency range was set from 100 kHz to 10 mHz. All the electrochemical measurements were carried out at room temperature.

Acknowledgements

This work is supported by National Natural Science Foundation of China (Grant No. 21373184).

References:

Figure Captions

Figure 1

Figure 2 (a) Raman spectra of GO film and RGO film. (b) C 1s XPS spectra of GO film. (c) C 1s XPS spectra of RGO film. (d) XRD patterns of as-prepared Mn_xO_y and MnO after annealing. (e) Mn 2p XPS spectra of RGO-MnO-RGO nanocomposite.

Figure 3 FESEM images of (a, b, c) pure RGO film; (d, e, f) RGO-MnO nanostructure; (g, h, i) RGO-MnO-RGO sandwich nanostructure.

Figure 4 (a, b, c) TEM images of RGO-MnO-RGO nanostructure; (d, e) HRTEM image (d) and SAED pattern (e) of RGO-MnO-RGO nanostructure.

Figure 5 (a) Representative CV curves of RGO-MnO-RGO electrode at a scan rate of 0.1 mV s^{-1};(b) CV curves of bare MnO electrode at a scan rate of 0.1 mV s^{-1}; (c) Cycling performance of RGO-MnO-RGO electrode(cycled at 0.5A g^{-1} and 1A g^{-1}), RGO-MnO electrode (cycled at 1A g^{-1}) and bare MnO electrode (cycled at 1A g^{-1}); (d) Discharge and charge voltage profiles of RGO-MnO-RGO electrode at a current density of 1 A g^{-1}; (e) Cycling performance of RGO-MnO-RGO electrode(at 0.2 A g^{-1} for the first five cycles and then 2 A g^{-1} or 5A g^{-1} for subsequent 500 cycles), RGO-MnO electrode (at 0.2 A g^{-1} for the first five cycles and then 5A g^{-1} for subsequent 100 cycles) and bare MnO electrode (at 0.2 A g^{-1} for the first five cycles and then 5A g^{-1} for subsequent 100 cycles); (f) Cyclic performance of RGO-MnO-RGO electrode cycled at 15A g^{-1} for 4000 cycles (at 0.2 A g^{-1} for the first five cycles).

Figure 6 (a) Rate performances of RGO-MnO-RGO and bare MnO electrodes; (b) Charge–discharge curves of bare MnO electrode at different current rates; (c) Charge–discharge curves of RGO-MnO-RGO electrode at different current rates; (d) Average discharge and charge potential of RGO-MnO-RGO and bare MnO electrodes at different current rates; (e) Ragone plots of RGO-MnO-RGO and bare MnO electrodes.

Figure 7

Fig. 1

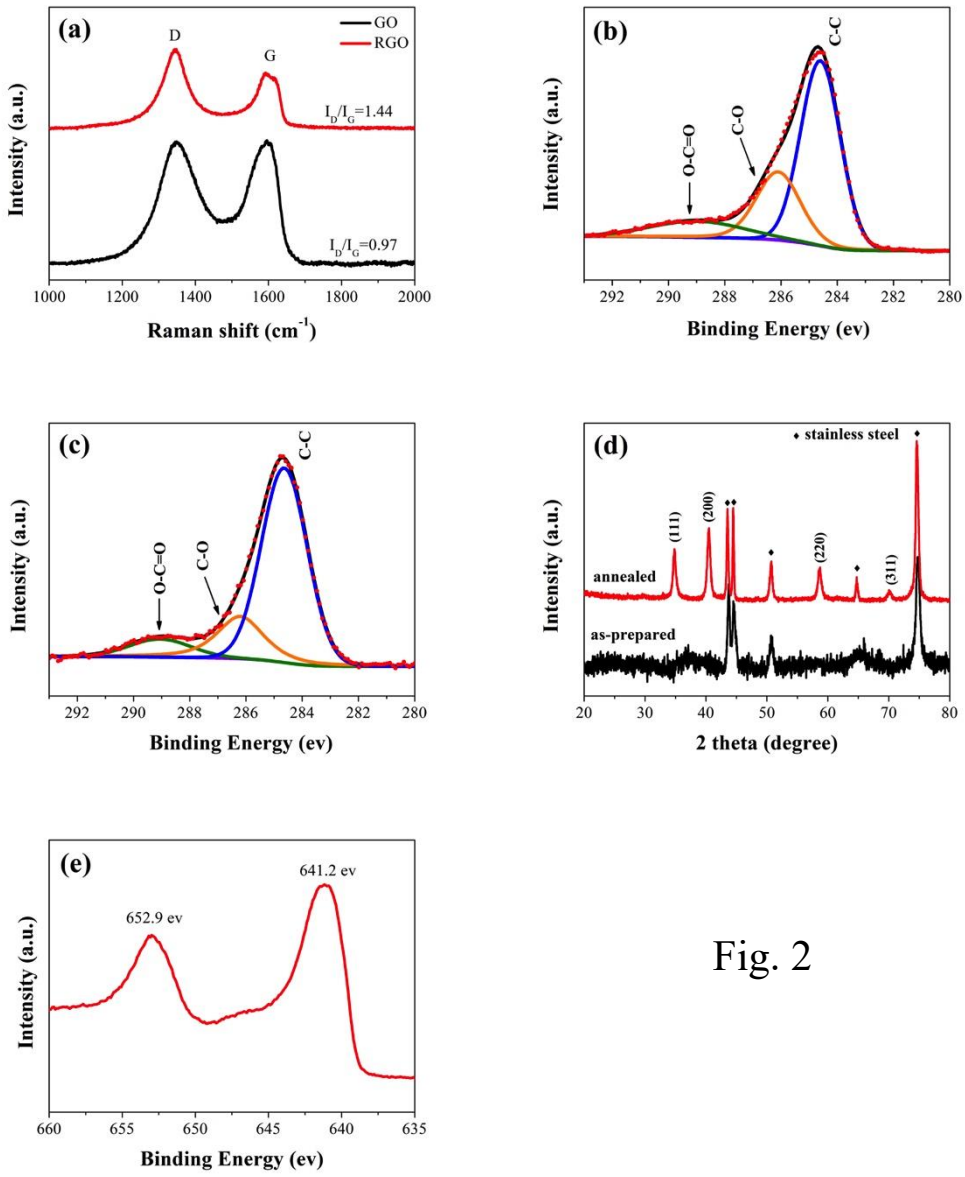
(a)
GO
RGO
D
G
I_D/I_G=1.44
I_D/I_G=0.97
Intensity (a.u.)
Raman shift (cm^{-1})
(b)
C-C
C-O
O-C=O
Intensity (a.u.)
Binding Energy (ev)
(c)
C-C
C-O
O-C=O
Intensity (a.u.)
Binding Energy (ev)
(d)
♦ stainless steel
(111)
(200)
(220)
(311)
annealed
as-prepared
Intensity (a.u.)
2 theta (degree)
(e)
641.2 ev
652.9 ev
Intensity (a.u.)
Binding Energy (ev)

Fig. 2

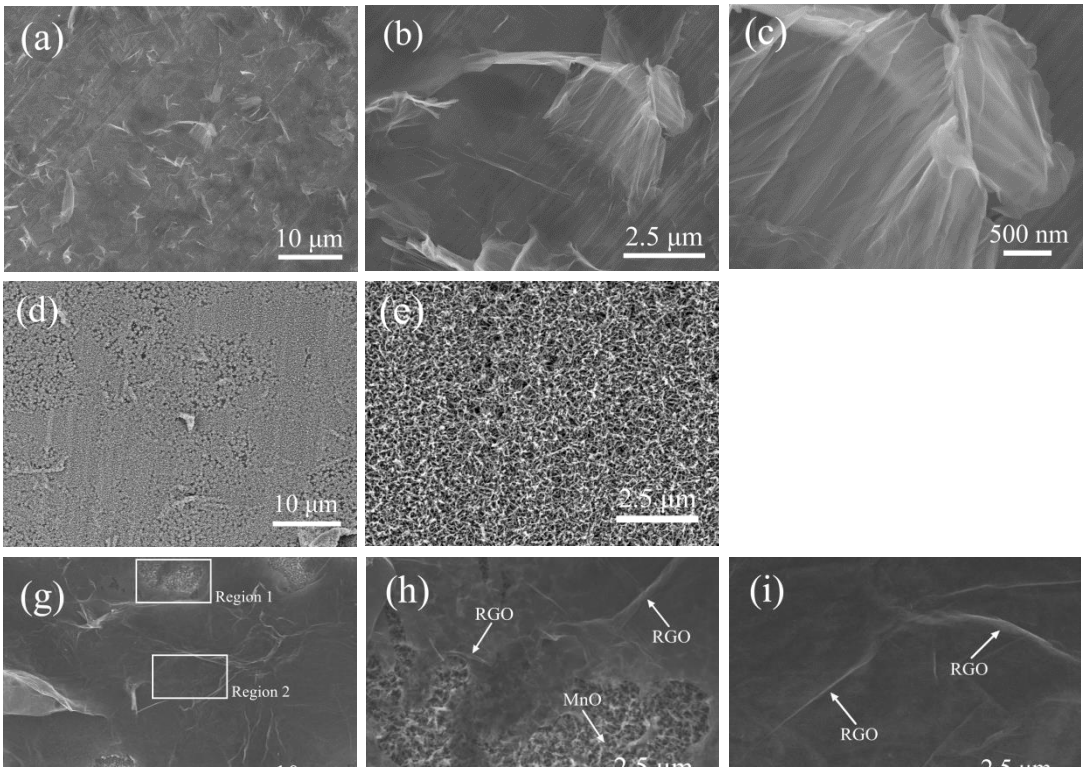
(a)
10 μm
(b)
2.5 μm
(c)
500 nm
(d)
10 μm
(e)
2.5 μm
(g)
Region 1
Region 2
(h)
RGO
RGO
MnO
(i)
RGO
RGO

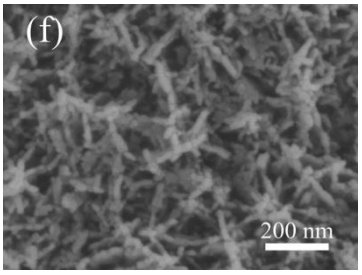
(f)
200 nm

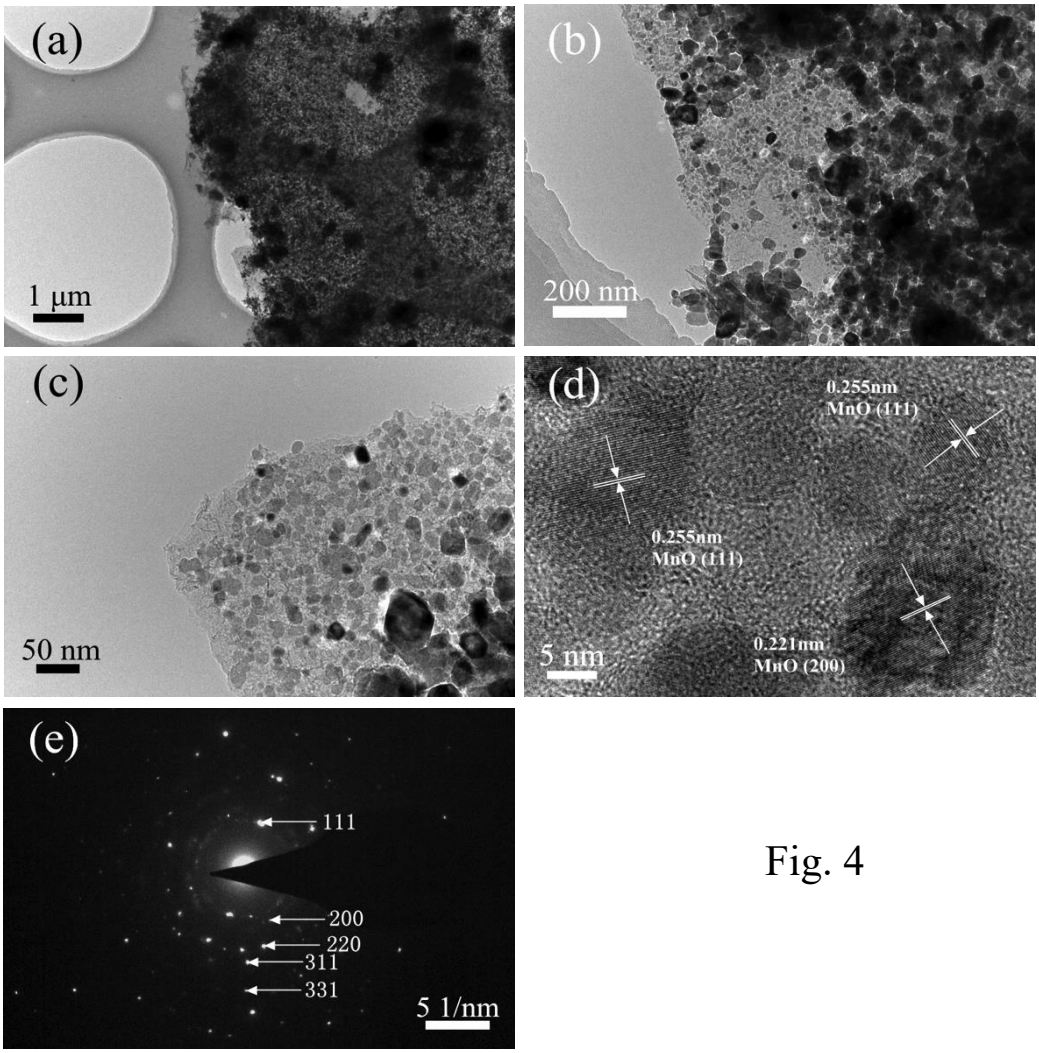
(a)
1 μm
(b)
200 nm
(c)
50 nm
(d)
0.255nm
MnO (111)
0.255nm
MnO (111)
5 nm
0.221nm
MnO (200)
(e)
111
200
220
311
331
5 1/nm

Fig. 4

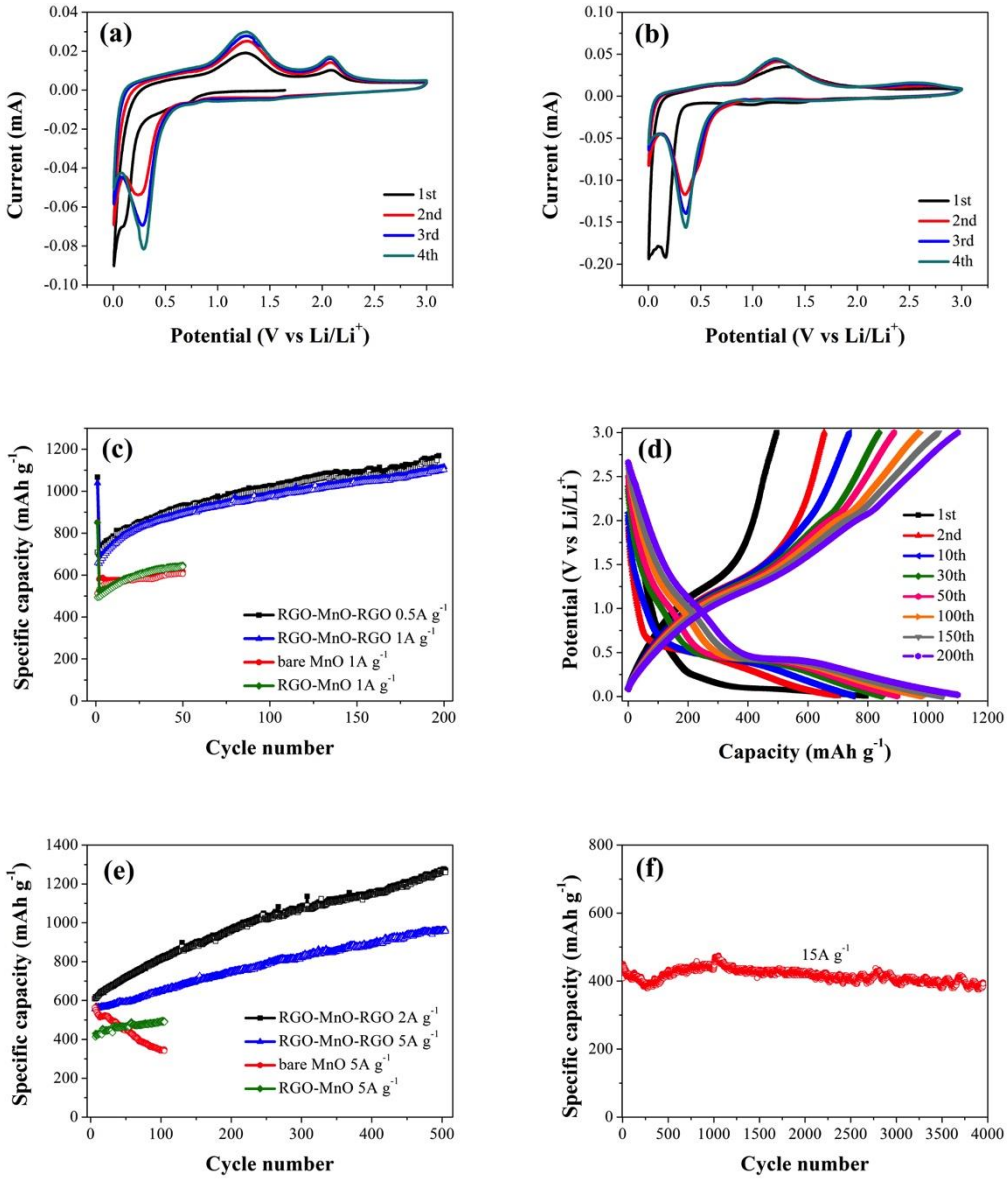
(a)
Current (mA)
Potential (V vs Li/Li+)
1st
2nd
3rd
4th
(b)
Current (mA)
Potential (V vs Li/Li+)
1st
2nd
3rd
4th
(c)
Specific capacity (mAh g-1)
Cycle number
RGO-MnO-RGO 0.5A g-1
RGO-MnO-RGO 1A g-1
bare MnO 1A g-1
RGO-MnO 1A g-1
(d)
Potential (V vs Li/Li+)
Capacity (mAh g-1)
1st
2nd
10th
30th
50th
100th
150th
200th
(e)
Specific capacity (mAh g-1)
Cycle number
RGO-MnO-RGO 2A g-1
RGO-MnO-RGO 5A g-1
bare MnO 5A g-1
RGO-MnO 5A g-1
(f)
Specific capacity (mAh g-1)
Cycle number
15A g-1

Fig. 5

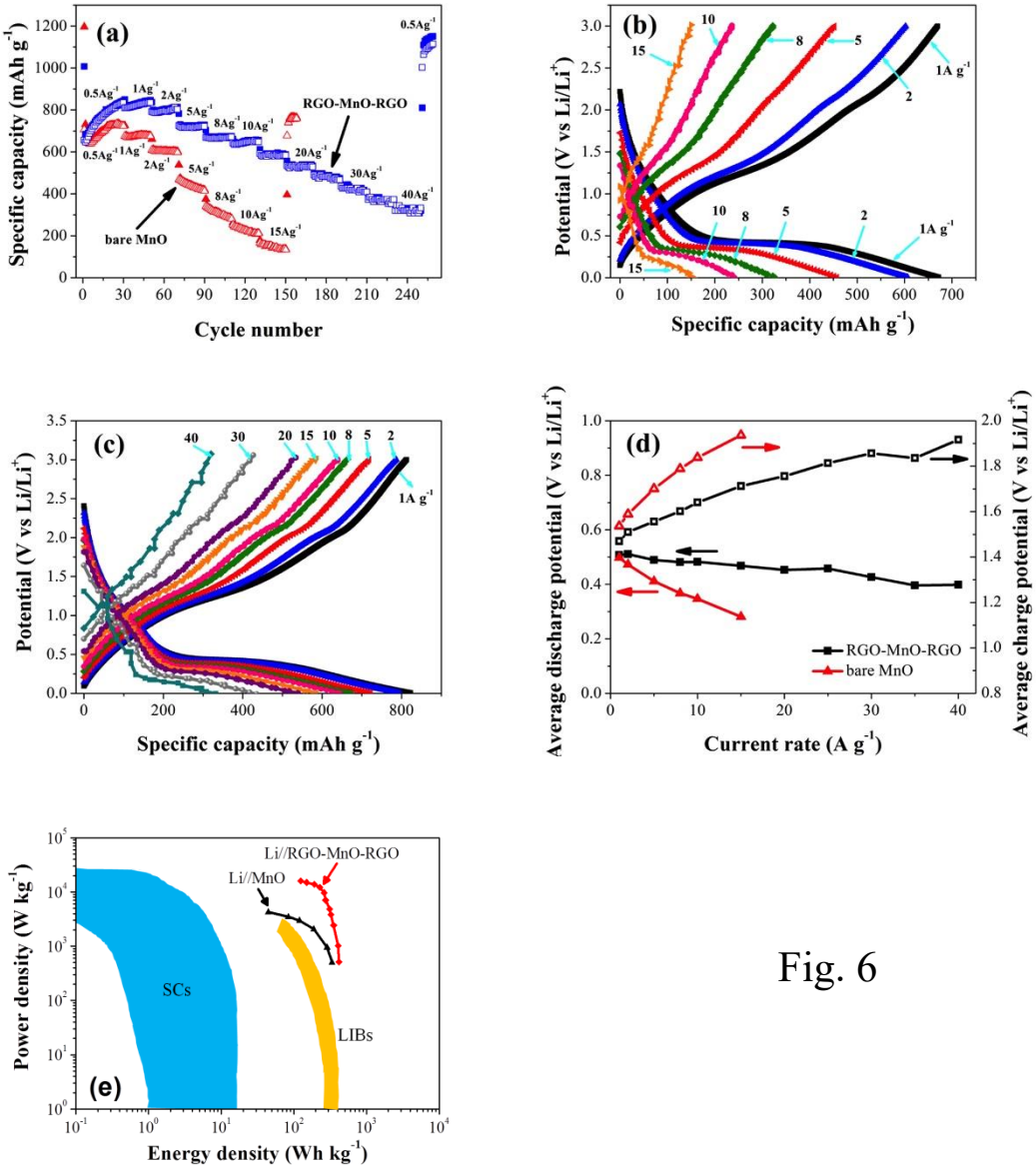
(a)
Specific capacity (mAh g-1)
Cycle number
RGO-MnO-RGO
bare MnO
(b)
Potential (V vs Li/Li+)
Specific capacity (mAh g-1)
1A g-1
(c)
Potential (V vs Li/Li+)
Specific capacity (mAh g-1)
1A g-1
(d)
Average discharge potential (V vs Li/Li+)
Average charge potential (V vs Li/Li+)
Current rate (A g-1)
RGO-MnO-RGO
bare MnO
(e)
Power density (W kg-1)
Energy density (Wh kg-1)
Li//RGO-MnO-RGO
Li//MnO
SCs
LIBs

Fig. 6

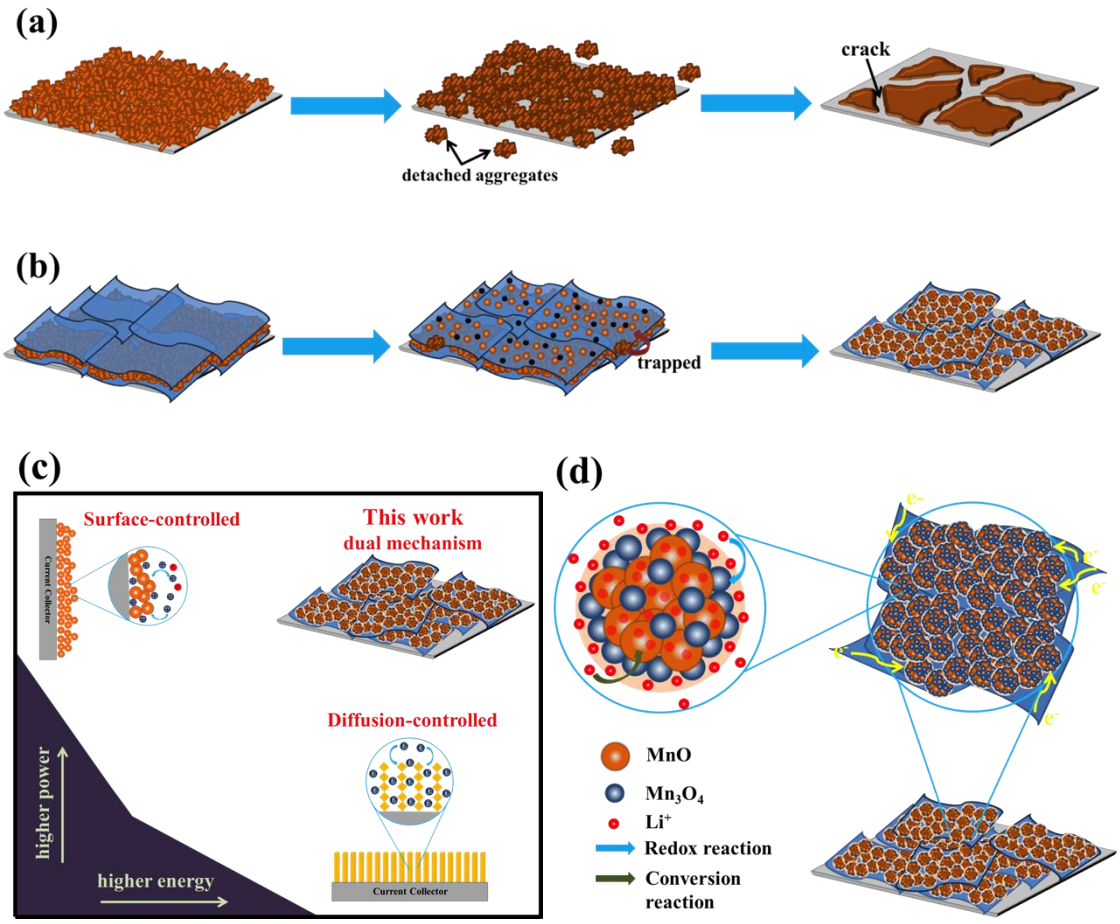
(a)
crack
detached aggregates
(b)
trapped
(c)
Surface-controlled
This work
dual mechanism
Diffusion-controlled
higher power
higher energy
Current Collector
(d)
MnO
Mn_3O_4
Li^+
Redox reaction
Conversion reaction

Fig. 1